J Mater Sci: Mater Electron **(2023) 34:1918**

Impacts of Mn-deficiency on the structure and physical properties of $GdMnO_3$ ceramics

Junling Wang[1], Haizeng Liu[2], Qinlong Shen[2], and Haiyang Dai[2,*]

[1] *Department of Traffic Information Engineering, Henan College of Transportation, Zhengzhou 450000, China*
[2] *School of Physics and Electronic Engineering, Zhengzhou University of Light Industry, Zhengzhou 450002, China*

Received: 6 August 2023
Accepted: 11 September 2023
Published online: 3 October 2023

ABSTRACT

The effects of Mn-deficiency on the structure, Mn ions valence, vacancy defects, magnetic and dielectric characteristics of $GdMn_{1-x}O_3$ ceramics synthesized by solid-state reaction were investigated. The results revealed that Mn-deficiency caused the lattice deformation, but had no effect on the orthorhombic perovskite structure of all $GdMn_{1-x}O_3$ samples. Raman analysis showed that Mn-deficiency induced octahedral distortions and lattice disorder and affected < Mn–O > length. XPS analysis implied that the valence state of Mn ion evolved in $GdMn_{1-x}O_3$ samples owing to the charge compensation. Positron annihilation lifetime spectroscopy revealed that the vacancy size and concentration increased with increasing Mn-deficiency concentration x. The properties measurements showed that the Mn-deficiency increased the relative dielectric permittivity and magnetization of $GdMnO_3$ system. The relationship between structure and performances was discussed in this paper.

1 Introduction

As a new type of multifunctional materials, multiferroic materials with magnetoelectric coupling between magnetic and ferroelectric orders exhibit new physical effects, which have broad potential application in transducers and other fields [1, 2]. They have drawn a great deal of interest recently. Among the many multiferroic materials, $GdMnO_3$ with perovskite structure has unique magnetic structure, ferroelectricity induced by magnetic orders, and significant intrinsic magnetoelectric coupling. $GdMnO_3$ shows an antiferromagnetism in the temperature of 46–22 K and a canted antiferromagnetism (weak ferromagnetism) at 7 K < T < 22 K due to the evolution of Mn^{3+} ordering, the long-range ordering of Gd moments begins to appear at ~7 K [3–5]. Although researchers have conducted a lot of studies on the structure and physical behavious of $GdMnO_3$ system, the physical mechanism of magnetic, ferroelectric, and magnetoelectric coupling is still up for debate, and the ferroelectric and magnetic phase-transition temperature needs to be further improved. The physical properties of $GdMnO_3$ system are regulated by lattice structure, chemical composition, spin structure, vacancy defects, etc. In the process of exploring the generation and regulation mechanism of ferroelectricity and magnetism, and optimizing the physical properties of $GdMnO_3$, it has been proved that adjusting the composition of B-site ions is an effective approach to effectively regulate

Address correspondence to E-mail: haiytai@126.com

https://doi.org/10.1007/s10854-023-11330-9

its microstructure and properties. Tiwari et al. [6] reported Cr doping on the evolution of structure and magnetic transitions in $GdMnO_3$, and found that the magnetization reversal with spin reorientation was associated with the competition between Mn, Cr and Gd ions. Pal et al. [7] explored the evolution of different magnetic orderings in $GdMnO_3$ systems by Fe^{3+} ions doping, and revealed that the magnetic structure of the systems was relegated by Fe^{3+}–Fe^{3+} interaction, Gd^{3+}–Fe^{3+} interaction, Mn magnetic structure, and Jahn–Teller distortion. In the W-substituted $GdMnO_3$ studied by Li et al. [8], W^{6+} ion substitution enhanced the polarization and magnetization of $GdMnO_3$ system through regulating ion valence state, grain/grain boundary resistivity, structural distortion, and micro-defect. Previous research revealed that a slight adjustment of B-site ions in $GdMnO_3$ might greatly influence the electric and magnetic characteristics. Considering that $GdMnO_3$ was placed at the phase boundary between the A-type antiferromagnetic order and the cycloidal spin order in the phase diagram of rare-earth manganites, the chemical disorder and defects caused by B-site deficiency may have some important influence on the multiferroicity of $GdMnO_3$ system. In this study, Mn-deficiency $GdMnO_3$ ceramics ($GdMn_{1-x}O_3$) were synthesized, and the impact of Mn-deficiency on the structure characteristics and physical performances of $GdMnO_3$ system was investigated.

Vacancy-type defects, which are unavoidable in materials, have distinct influence on the physical characteristics of materials [9]. Perovskite materials can tolerate certain level of structural defects. $GdMnO_3$ with perovskite structure could accommodate certain concentration of anion and cation vacancies. Positron annihilation technology can clearly provide detailed information about the concentration, size, and type of vacancy defects at the atomic scale of materials. Therefore, positron annihilation technique was employed in this work to derive the characteristics of vacancy-type defects in $GdMn_{1-x}O_3$ with Mn-deficiency, and the relation between structure and physical properties of $GdMn_{1-x}O_3$ ceramic was studied.

2 Experimental details

$GdMn_{1-x}O_3$ ceramics ($x = 0.00$, 0.02, 0.05, 0.08, and 0.10) were synthesized by the solid-state reaction. Using alcohol as the medium, the dried powders Gd_2O_3 (99.99%) and Mn_3O_4 (99.99%) with proper stoichiometric ratio were ball milled for 24 h at 150 rpm for homogenous mixing. The ball-milled mixtures were calcined twice at 1000 and 1250 °C for 24 h, respectively. After each calcination, the calcined powders were ball milled for 2 h at 150 rpm to obtain powders with finer particles. Finally, the twice calcined powders were pressed into a wafer (φ11mm × 1.5 mm) under 10 MPa.

To investigate the phase structure of the $GdMn_{1-x}O_3$ ceramics, X-ray powder Diffraction with a Bruker D8 diffractometer using Cu-$k\alpha$ radiation within a 2θ range of 20°-70° was performed. To obtain the vibrational modes information, a Raman microscope (Renishaw, United Kingdom) with 532 nm excitation laser was employed. The element composition, valence state and relative content were determined by X-ray photoelectron spectroscopy (XPS, Esca lab 250XI). To determine the cation vacancy information in the samples, positron annihilation lifetime spectroscopy (PALS) measurement was carried out utilizing 13 Ci ^{22}Na as the positron source. An Agilent HP 4194 A impedance analyzer was employed to analyze the dielectric properties in the 100 Hz-10 MHz frequency range. The magnetic behaviors of the $GdMn_{1-x}O_3$ were measured using a Physical property measuring system (Quantum Design).

3 Results and discussion

X-ray powder diffraction patterns of $GdMn_{1-x}O_3$ ($x = 0.00$–0.10) ceramics were shown in Fig. 1. The patterns for all ceramics matched perfectly with the standard card of $GdMnO_3$ without any other impurity phases [10], indicating that a series of $GdMn_{1-x}O_3$ polycrystalline samples with single-phase orthorhombic perovskite structure (space group P*bnm*) were synthesized. The results proved that the deficiency of Mn ions in $GdMnO_3$ had no influence on the type of crystal structure. The dominant peaks in all ceramics exhibited the characteristics of high intensity and narrow width, which demonstrated the $GdMn_{1-x}O_3$ ceramics possessed excellent crystallinity.

To precisely analyze the influence of Mn-deficiency on lattice properties, the XRD data was refined using the GSAS program. Table 1 displayed the lattice parameters and cell volume of the $GdMn_{1-x}O_3$. The weighted difference sum of squares (χ^2) was within the accepted level, demonstrating the credible of refinement results. The lattice parameters of

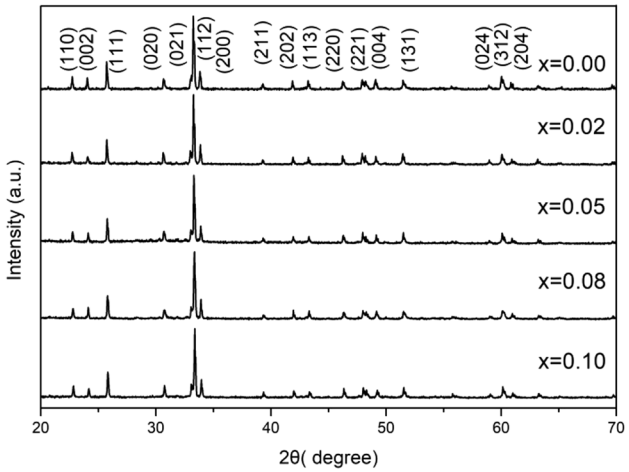

Fig. 1 X-ray diffraction patterns of the $GdMn_{1-x}O_3$ ceramics

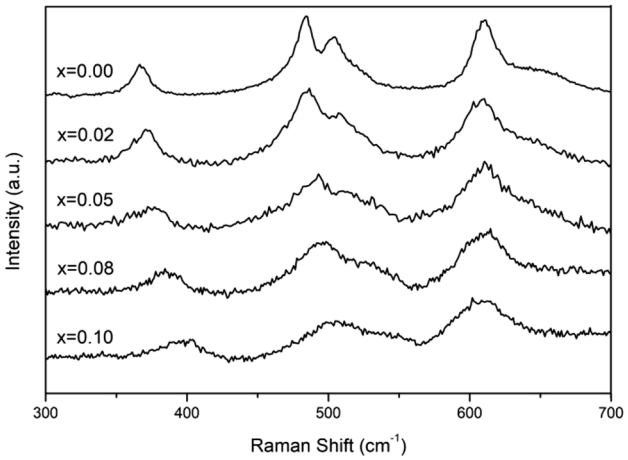

Fig. 2 Raman spectra of $GdMn_{1-x}O_3$ samples

Table 1 Refined lattice parameters of the $GdMn_{1-x}O_3$ structures

Mn-deficiency content x	a (Å)	b (Å)	c (Å)	Volume (Å^3)	χ^2
0.00	5.31336	5.84312	7.43695	230.892	1.109
0.02	5.31193	5.84291	7.43731	230.833	1.092
0.05	5.30965	5.84016	7.43896	230.676	1.193
0.08	5.30756	5.83857	7.44173	230.609	1.385
0.10	5.30468	5.83876	7.44297	230.529	1.059

the stoichiometric $GdMnO_3$ samples ($x = 0.00$) deviated from the published ICSD values by less than 0.5 percent, showing that the refinement results of the $GdMn_{1-x}O_3$ samples were reliable. Compared with the $x = 0.00$ samples, the cell volume of Mn-deficiency samples was slightly reduced, indicating Mn-deficiency induced slight lattice shrinkage. This might be due to the introduction of Mn vacancies and the generation of Mn^{4+} (0.53 Å) ions with a smaller ionic radius than that of Mn^{3+} (0.58 Å) [11].

Raman spectroscopy measurements were performed to investigate the impact of Mn-deficiency on the vibrational modes information for $GdMn_{1-x}O_3$ samples. Figure 2 showed the Raman spectra of $GdMn_{1-x}O_3$ compounds. It has been predicted that the $GdMnO_3$ with orthorhombic perovskite structure had a total of 24 Raman modes ($7A_g + 7B_{1g} + 5B_{2g} + 5B_{3g}$) [12, 13]. Nevertheless, since the majority of Raman vibrational modes were too weak to be detected, as shown in Fig. 2, only four Raman vibrational modes were observed within the frequency range of 300–800 cm^{-1}. The Raman vibration peaks situated at ~ 484.3 and ~ 610.3 cm^{-1} were assigned to the antisymmetric and symmetric Jahn–Teller stretching modes, respectively. The other peaks located at ~ 365.3 and ~ 504.6 cm^{-1} were associated to the tilt and bending of the MnO_6 octahedron, respectively. The positions of Raman vibrational modes matched to the values in earlier research [12, 13]. Compared with the stoichiometric $GdMnO_3$ ($x = 0.00$), the positions of Raman modes located at ~ 365.3 and 504.6 cm^{-1} were slightly moved towards the higher wave number, the mode at ~ 484.3 cm^{-1} corresponding to the < Mn–O > length also shifted towards the higher wave number, while the mode at 610.3 cm^{-1} arised from < Gd–O > vibration did not change significantly. The results showed that Mn-deficiency had obvious effect on the structure of the MnO_6 octahedron and < Mn–O > length, but had little effect on the < Gd–O > bond. This might be attributed to the stress and the change of the Mn^{3+}/Mn^{4+} mixed structure in the samples caused by Mn-deficiency. It could also been detected the broadening of Raman peaks caused by the deficiency of manganese. The broadening characteristic indicated that Mn-deficiency induced lattice disorder in $GdMn_{1-x}O_3$, because the width of Raman peaks was related to the lattice disorder in $GdMnO_3$ [14]

The influence of Mn-deficiency on the chemical states of elements in $GdMn_{1-x}O_3$ ceramics was investigated by utilizing XPS. Figure 3 illustrated the XPS survey spectrum of $GdMn_{0.95}O_3$ samples. Carbon peaks located at binding energy of 284.8 eV were due to the adventitious carbon from atmosphere, which

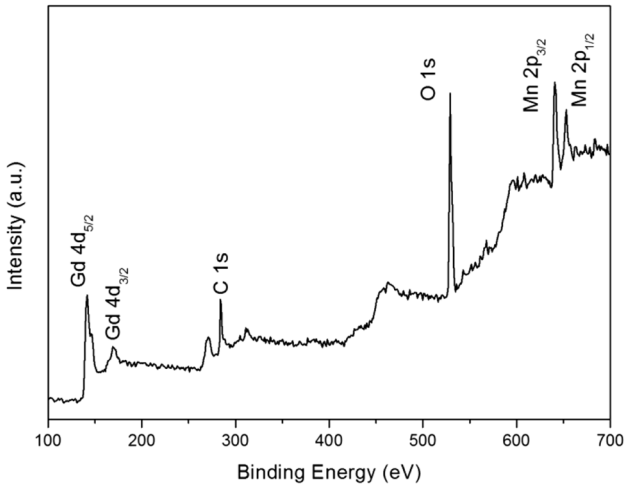

Fig. 3 The XPS survey spectrum of the $GdMn_{0.95}O_3$ ceramics

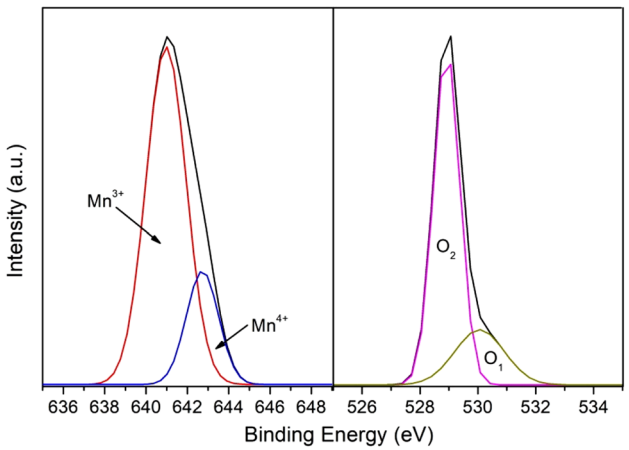

Fig. 4 The deconvolution of Mn $2p_{3/2}$ and O1s spectra of the $GdMn_{0.95}O_3$ samples

could be utilized for calibrating each spectrum. The XPS survey spectrum showed in Fig. 3 revealed that elements Gd, Mn, O, and C could be identified in the samples devoid of impurity elements. Figure 4 illustrated the high-resolution spectra of Mn $2p_{3/2}$ for $GdMn_{0.95}O_3$ ceramics. The Mn $2p_{3/2}$ XPS spectra for all samples were fitted into two sub-peaks at ~ 640.5 and 642.2 eV, which were corresponding to Mn^{3+} and Mn^{4+} ions [4, 15], respectively. The peak area could be used to calculate the relative amount of Mn ions with different valences. The relative content of Mn^{4+} in the $GdMn_{1-x}O_3$ samples was shown in Table 2 and Fig. 5. With the increase of Mn-deficiency content, Mn^{4+} content increased gradually. It revealed that the deficiency of Mn ions resulted in the formation of

Table 2 Relative content of Mn^{4+} and O_{II}/O_I in the $GdMn_{1-x}O_3$ samples

Mn-deficiency content x	$x=0.00$	$x=0.02$	$x=0.05$	$x=0.08$	$x=0.10$
Mn^{4+}	8.5%	12.7%	18.3%	21.3%	25.5%
O_{II}/O_I	0.321	0.334	0.310	0.342	0.314

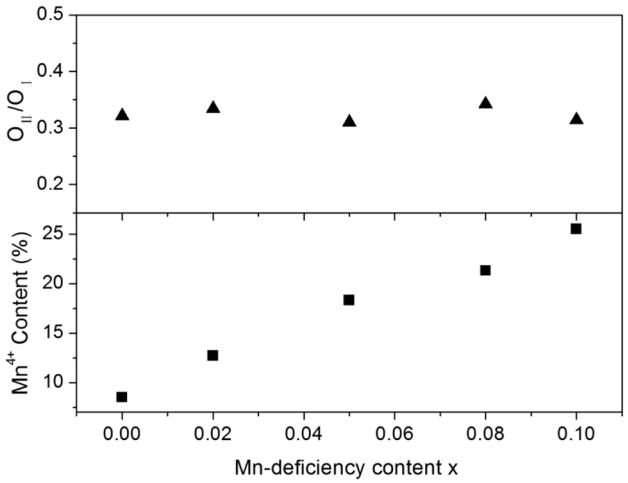

Fig. 5 Mn^{4+} content and O_{II}/O_I in $GdMn_{1-x}O_3$ as a function of Mn-deficiency content

high-valent Mn ions (Mn^{4+}) due to the charge compensation [16]. The O1s spectra of all $GdMn_{1-x}O_3$ shown in Fig. 4 could also be deconvoluted into two sub-peaks. The fitted peaks with binding energies of ~ 529.3 (O_I) and ~ 531.4 eV (O_{II}) represented the lattice oxygen and oxygen vacancies [4, 15], correspondingly. As shown in Table 2, the ratio of O_{II}/O_I in the $x = 0.00$, 0.02, 0.05, 0.08, and 0.10 samples were approximately 0.321, 0.334, 0.310, 0.342, and 0.314, respectively. This signified that the deficiency of Mn ions had no significant influence on the oxygen vacancy concentration for the $x = 0.00$–0.10 samples. The change trends of Mn^{4+} and oxygen vacancies concentration showed that deficiency of Mn mainly causes the conversion of Mn valence states.

The feature of vacancy defect in $GdMn_{1-x}O_3$ ceramic samples was characterized by positron annihilation spectroscopy. Typically, positron annihilation lifetime spectroscopy of ceramics was decomposed into three lifetime components τ_1, τ_2, and τ_3 with the corresponding intensities I_1, I_2, and I_3 ($I_1 + I_2 + I_3 = 1$) after subtracting source composition and background. The

intensity I_3 was relatively small ($I_3 < 0.9\%$), it will be ignored in the following discussion, and I_1 and I_2 were re-normalized ($I_1 + I_2 = 1$). The positron annihilation lifetime parameters of $GdMn_{1-x}O_3$ samples were listed in Fig. 6. The short lifetime τ_1 represented the positrons annihilation in perfect lattice. The long lifetime τ_2, representing the open volume of vacancy defects, was due to the annihilation of positrons at defects [16–18]. The corresponding intensities I_1, I_2 reflected the relative concentrations of the components. According to the two-state trapping model, the average positron lifetime τ_{av}, which also characterized the defect concentration in materials, could be calculated using the following equation [16]:

$$\tau_{av}=\tau_1.I_1 + \tau_2.I_2 \quad (1)$$

The local electron density n_e was calculated using the following formula [16]:

$$n_e = \frac{1}{\pi r_0^2 c \tau_{av}} \quad (2)$$

where r_0 is the classical electron radius, c is the velocity of light.

Figure 6 depicted the values of τ_1, τ_2, τ_{av}, and I_2 with Mn-deficiency content x. It was clear that τ_1 decreased with Mn-deficiency content x. This was compatible with the XRD analysis. The positron annihilation lifetime was inversely proportional to the electron density of the positron annihilation, and the XRD results indicated that Mn-deficiency induced lattice shrinkage in $GdMn_{1-x}O_3$. Therefore, the increase of electron density in the lattice caused the decrease of τ_1. The reported theoretical positron lifetimes for Tb-site and Mn-site monovacancy defects in $TbMnO_3$ are 259 and 199 ps, respectively [19]. The structure of $TbMnO_3$ is identical with that of $GdMnO_3$, and Gd and Tb ions are adjoining members of the lanthanum series. Therefore, the positron lifetimes for Gd-site and Mn-site monovacancy defects in $GdMnO_3$ should be close to 259 and 199 ps, respectively. The experimental value of τ_2 for the $GdMn_{1-x}O_3$ ceramics was in the range of 230–239 ps. Therefore, the type of cationic vacancies in the $GdMn_{1-x}O_3$ material was Mn vacancies. The long lifetime τ_2 increased with increasing x, as indicated in Fig. 6a. Because higher τ_2 values in solid materials reflected the larger size of vacancy defects in the samples, the Mn-deficiency caused an increase in vacancies size of $GdMn_{1-x}O_3$ ceramics. As shown in Fig. 6b, both I_2 and τ_{av} increased with Mn-deficiency content from 0.00 to 0.10. It meant that the concentration vacancies increased with Mn-deficiency content, which might be explained by the deficiency of cations and the lattice shrinkage in the $GdMn_{1-x}O_3$ samples. According to formula (2), the variation of τ_{av} would cause the change of n_e, that is, Mn-deficiency modulated the electron density of the $GdMn_{1-x}O_3$ samples.

To investigate the impact of Mn-deficiency on the dielectric properties of $GdMn_{1-x}O_3$, the variation of relative dielectric permittivity (ε_r) and dielectric loss (tanδ) with frequency in the range of 100 to 1.0×10^6 Hz were measured at room temperature

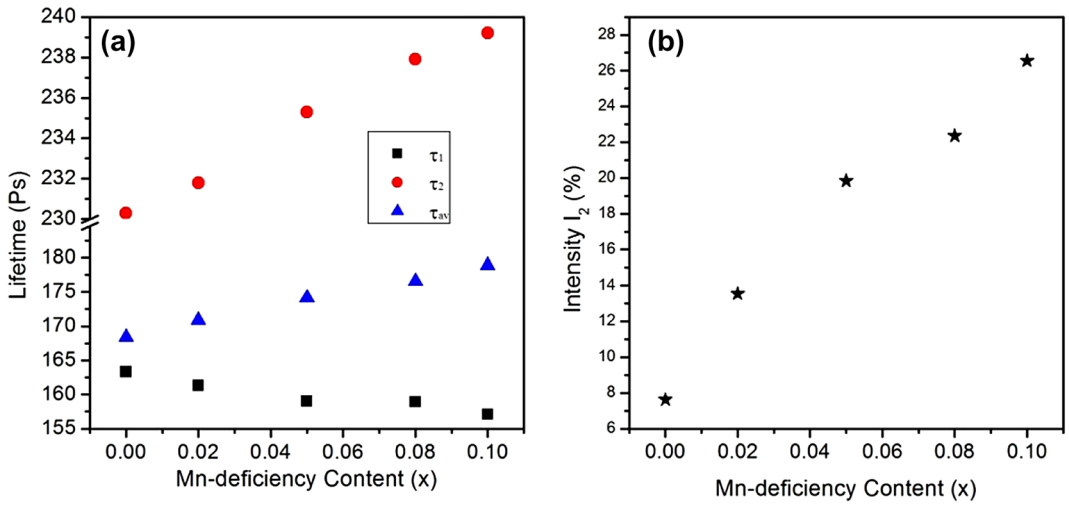

Fig. 6 The positron lifetimes τ_1, τ_2, τ_{av}, and intensity I_2 of the $GdMn_{1-x}O_3$ samples

and showed in Fig. 7. The curves in Fig. 7a revealed the strong frequency dispersion of relative dielectric permittivity for all samples. As the measurement frequency increased, the relative dielectric permittivity rapidly decreased by several orders of magnitude. This is mostly owing to many types of polarization (electronic and ionic displacement polarization, space-charge polarization, interfacial polarization etc.) presented in the ceramics, and only part of the polarizations responded to frequency in the high frequency range. As the Mn-deficiency content increased, the relative dielectric permittivity of $GdMn_{1-x}O_3$ samples showed an increasing trend, the relative dielectric permittivity of $x = 0.10$ sample (1288.2) was 16.1 times that of $x = 0.00$ sample (79.9) when the test frequency was 10^6 Hz. This was likely to result from the polar arrangement of electrons on the mixed valence structure of Mn^{3+}/Mn^{4+}, displacement polarization induced by structural distortion, and change of electron density [20]. Figure 7b showed the frequency variation of the dielectric loss (tanδ) for $GdMn_{1-x}O_3$ samples. With the increase of frequency, the variation trend of tanδ for $GdMn_{1-x}O_3$ samples was similar to that of relative dielectric permittivity. tanδ of Mn-deficiency samples was higher that of the stoichiometric $GdMnO_3$, which should be mainly attributed to the leakage current induced by the mixed valence structure of Mn^{3+}/Mn^{4+}. In conclusion, Mn-deficiency could be used to effectively regulate the dielectric properties of $GdMnO_3$ samples; the relative dielectric permittivity of $GdMn_{0.90}O_3$ sample could reach 1288.2.

Figure 8 depicted the temperature dependence of the magnetization for $GdMn_{1-x}O_3$ samples in zero-field-cooled (ZFC) and field-cooled (FC) conditions under magnetic field of 1 kOe between 5 and 300 K. The illustration was the partial enlargement. Previously, it has revealed that $GdMnO_3$ with paramagnetic characteristics at room temperature underwent intricate magnetic transitions at lower temperature due to the change in the spin structure of Gd^{3+} and Mn^{3+} and the interaction between Gd^{3+} and Mn^{3+} sublattices. The ZFC and FC curves of $GdMn_{1-x}O_3$ samples showed in Fig. 8 coincided at high temperatures, while a distinct bifurcation could be observed at lower temperatures, indicating that the $GdMn_{1-x}O_3$ system has both antiferromagnetism and ferromagnetism at low temperature. According to literature [3, 4, 21], the first anomaly at ~ 44 K in the ZFC curve of $GdMnO_3$ was caused by the transition from a paramagnetic to an incommensurate antiferromagnetic due to the appearance of Mn^{3+} spin ordering. However, such anomaly could not be detected in the ZFC curves of all samples, which was mainly due to the masking effect of great paramagnetic signal generated by Gd^{3+} moment. At ~ 23 K, the second anomaly occurred due to the canted spin ordering of Mn^{3+}, which arose from canted antiferromagnetic ordering associated with weak ferromagnetism. The third anomaly at ~ 8 K in the ZFC curve was ascribed to the onset of Gd^{3+} ordering in the $GdMnO_3$. As shown in the insets of Fig. 8, the temperature of the second and third anomalies did not change significantly for all $GdMn_{1-x}O_3$ samples, but the magnetization of

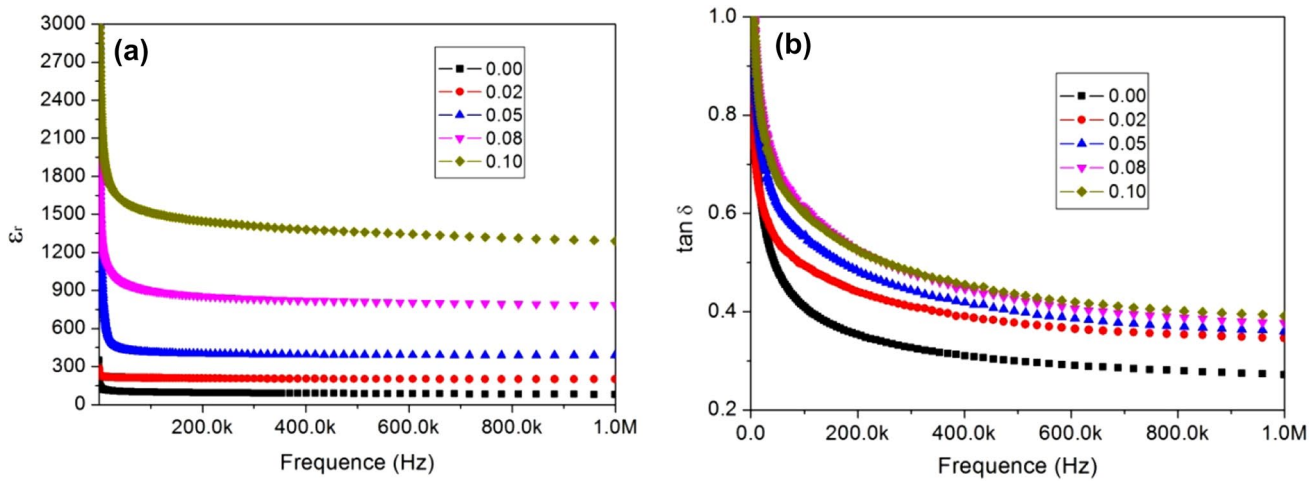

Fig. 7 The frequency dependence of the relative dielectric permittivity (**a**) and dielectric loss (**b**) of the $GdMn_{1-x}O_3$ samples

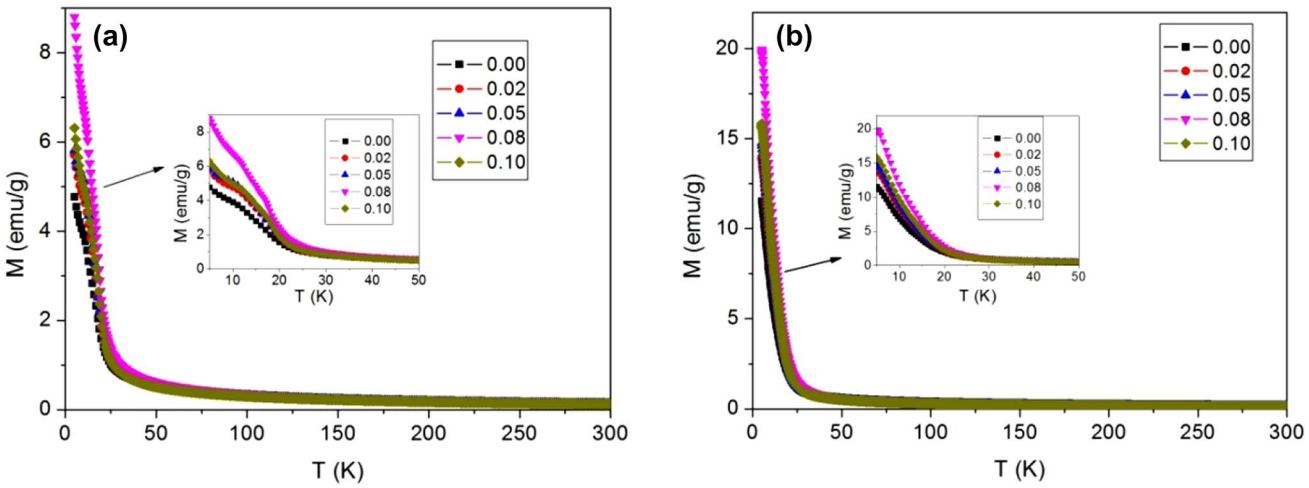

Fig. 8 Temperature dependence of the ZFC (*a*) and FC (*b*) magnetization curves for the $GdMn_{1-x}O_3$ samples. The illustration is a partial enlargement

Mn-deficiency samples was higher than that of the stoichiometric $GdMnO_3$. It indicated that Mn-deficiency did not affect the ordering temperature of Gd and Mn moments, but it improved the magnetization. In the FC curves, the anomaly at a temperature of ~ 23 K could only be observed, which might arise from the increased local magnetic field at the Gd site due to the ferromagnetic ordering of the Mn^{3+} moment. To further investigate the magnetic interaction, the ZFC curve was fitted using the Curie–Weiss law, the calculated Curie–Weiss temperatures of the $GdMn_{1-x}O_3$ ceramics were negative, indicating that the antiferromagnetic interaction was dominant in $GdMn_{1-x}O_3$ ceramics [21].

Figure 9 showed the hysteresis loops of $GdMn_{1-x}O_3$ samples at $T = 5$ K and 30 K. At 30 K, the magnetization of all $GdMn_{1-x}O_3$ samples showed a linear change, indicating that all the samples had anti-ferromagnetic characteristics. At 5 K, all of the samples showed obvious hysteresis loops, indicating ferromagnetic characteristics at this temperature. The maximum magnetization of $x = 0.00$, 0.02, 0.05, 0.08, and 0.10 samples were 28.1, 30.2, 32.2, 40.6, and 30.5 emu/g, respectively. The remanent magnetizations were 7.4, 9.1, 9.7, 11.8, and 8.7 emu/g, respectively. It was obvious that the magnetization showed a trend of first increasing and then decreasing. On one hand, $GdMn_{1-x}O_3$ samples showed ferrimagnetic properties at 5 K, and the insertion of

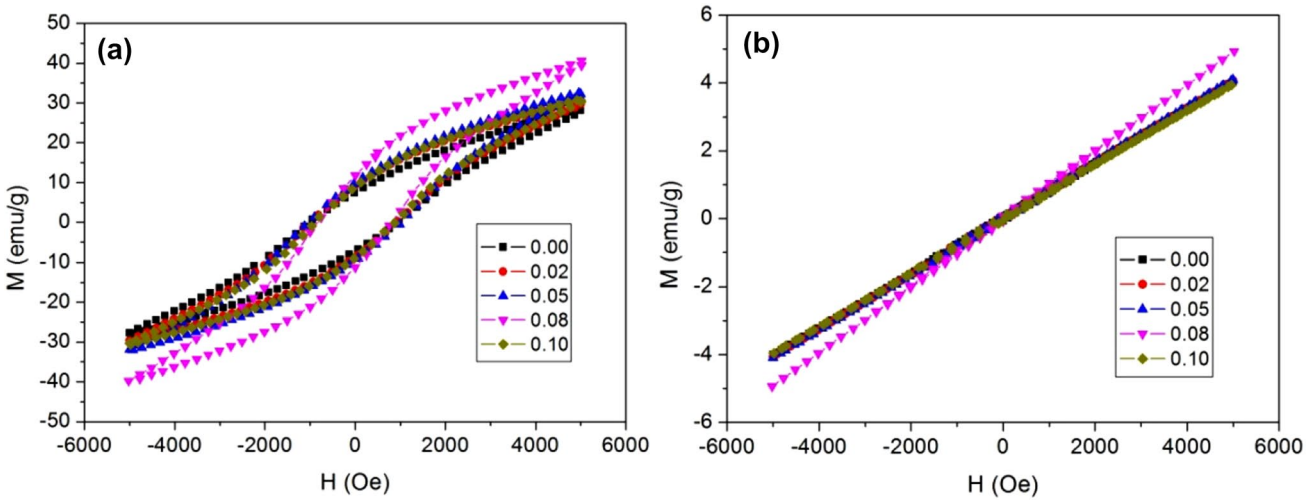

Fig. 9 Magnetization as a function of the applied field (*M–H*) in the $GdMn_{1-x}O_3$ samples at 5 K (**a**) and 30 K (**b**)

cation vacancies in ferrimagnetic orderings enhanced the magnetization. Moreover, $GdMnO_3$ exhibited spiral spin magnetic configurations at low temperatures, and the structural distortion induced by Mn-deficiency could suppress the spiral spin magnetic configurations and led to an improvement of magnetization. In addition, the interaction between Mn^{3+} and Mn^{4+} led to ferromagnetic configuration, improving the magnetization. Therefore, the magnetization was improved with increasing Mn-deficiency content x from 0.00 to 0.08. However, Mn-deficiency would induce dilution effect and decrease the magnetization of $GdMn_{1-x}O_3$ samples. Therefore, the magnetization was decreased for the $GdMn_{0.10}O_3$ sample.

4 Conclusions

In this paper, the structure, vacancy defects, magnetic and dielectric properties of $GdMn_{1-x}O_3$ polycrystalline samples prepared by solid phase reaction were studied. Microstructure tests showed that Mn-deficiency could affect the lattice structure and cause lattice distortion. The XPS results showed that the Mn-deficiency introduced more Mn^{4+} in $GdMn_{1-x}O_3$ polycrystalline samples. The results of the positron annihilation lifetime spectroscopy showed that the vacancy concentration of Mn-deficiency samples increases greatly. The performances test showed that the Mn-deficiency samples had higher relative dielectric permittivity and dielectric loss. The magnetic measurements showed that the antiferromagnetic interaction was dominant in $GdMn_{1-x}O_3$ compounds; Mn-deficiency improved the magnetization of the $GdMnO_3$ system due to the vacancy defects, lattice distortion, and interaction between Mn^{3+} and Mn^{4+}.

Acknowledgements

This work is supported by the National Natural Science Foundation of China (12275242), and the Natural Science Foundation of Henan Province (212300410092).

Author contributions

JW contributed to material preparation, investigation, and writing-original draft; HL contributed to material preparation, data collection, and validation; QS contributed to validation and analysis; and HD contributed to resources, conceptualization, investigation, and writing—original draft. All authors read and approved the final manuscript.

Data availability

The datasets generated during and/or analyzed during the current study are available from the corresponding author on reasonable request.

Declarations

Conflict of interest There is no conflict of interest to declare.

References

1. A. Bagri, D.M. Phase, R.J. Choudhary, Acta Mater. **255**, 119091 (2023)
2. V. Nagendar, N. Raju, S. Shravan Kumar Reddy, M. Sreenath Reddy, C. Gopal Reddy, P. Yadagiri Reddy, J. Mater. Sci. Mater. Electron. **34**, 1535 (2023)
3. A. Pal, W. Prellier, P. Murugavel, J. Phys. Condens. Matter **30**, 125801 (2018)
4. A. Pal, P. Murugavel, J. Appl. Phys. **123**, 234102 (2018)
5. P. Tiwari, D. Gangwar, C. Rath, New J. Chem. **45**, 13608 (2021)
6. P. Tiwari, S. Kumar, C. Rath, RSC Adv. **9**, 39871 (2019)
7. A. Pal, C. Dhana Sekhar, A. Venimadhav, P. Murugavel, J. Phys. Condens. Matter **29**, 405803 (2017)
8. T. Li, H.Z. Liu, J. Chen, D.W. Liu, H.Y. Dai, J. Mater. Sci. Mater. Electron. **33**, 25920 (2022)
9. D.J. Keeble, S. Singh, R.A. Mackie, M. Morozov, S. McGuire, D. Damjanovic, Phys. Rev. B **76**, 144109 (2007)
10. A. Rasras, R. Hamdi, S. Mansour, A. Samara, Y. Haik, J. Phys. Chem. Solids **149**, 109798 (2021)
11. J.A. Dean, Lange's Handbook of Chemistry, 15th edn. (McGraw-Hill, New York, 1999), pp. 4.30–4.43.
12. D. Singh, R. Gupta, K.K. Bamzai, J. Mater. Sci. Mater. Electron. **28**, 5295 (2017)
13. N.D. Todorov, M.V. Abrashev, V.G. Ivanov, G.G. Tsutsumanova, V. Marinova, Y.Q. Wang, M.N. Iliev, Phys. Rev. B **83**, 224303 (2011)

14. R. Vilarinho, E.C. Queiros, A. Almeida, P.B. Tavares, M. Guennou, J. Kreisel, J. Agostinho Moreira, J. Solid State Chem. **228**, 76 (2015)
15. P. Pant, H. Agarwal, S. Bharadwaj, M.A. Shaz, Mater. Chem. Phys. **290**, 126518 (2022)
16. T.D. Zhang, W.F. Pan, S.T. Ning, N. Qi, Z.Q. Chen, X.L. Su, X.F. Tang, Adv. Funct. Mater. **33**, 2213761 (2023)
17. V.J. Ghosh, B. Nielsen, T. Friessnegg, Phys. Rev. B **61**, 207 (2000)
18. K. Siemek, A. Olejniczak, L.N. Korotkov, P. Konieczny, A.V. Belushkin, Appl. Surf. Sci. **578**, 151807 (2022)
19. D.J. Keeble, S. Wicklein, R. Dittmann, L. Ravelli, R.A. Mackie, W. Egger, Phys. Rev. Lett. **105**, 226102 (2010)
20. N. Ikeda, H. Ohsumi, K. Ohwada, K. Ishii, T. Inami, K. Kakurai, Y. Murakami, K. Yoshii, S. Mori, Y. Horibe, H. Kito, Nature **436**, 1136 (2005)
21. A. Nandy, A. Roychowdhury, T. Kar, D. Das, S.K. Pradhan, RSC Adv. **6**, 20609 (2016)